Long-wavelength gravity field constraint on the lower mantle viscosity in North America

J.M. Reusen[1], B.C. Root[1], W. Szwillus[2], J. Fullea[3,4], W. van der Wal[1]

[1]Astrodynamics & Space Missions, Delft University of Technology, The Netherlands
[2]Department of Geosciences, Kiel University, Kiel, Germany
[3]Dublin Institute for Advanced Studies, School of Cosmic Physics, Dublin, Ireland
[4]Department Física Tierra y Astrofísica, Universidad Complutense de Madrid, Spain

Key Points:

- We model the gravity anomaly in Laurentia resulting from crustal- and lithospheric inhomogeneities, GIA and Dynamic Topography (DT).
- The gravity anomaly is most sensitive the lower mantle viscosity in models for GIA and DT.
- Best fitting models have a lower mantle viscosity larger than 10^{22} Pa s.

Corresponding author: Jesse Reusen, j.m.reusen@tudelft.nl

Abstract

The long-wavelength negative gravity anomaly over Hudson Bay coincides with the area depressed by the Laurentide ice sheet during the Last Glacial Maximum, suggesting that it is, at least partly, caused by Glacial Isostatic Adjustment (GIA). Additional contributions to the static gravity field stem from dynamic topography and density anomalies in the subsurface. Previous estimates of the contribution of GIA to the gravity anomaly range from 25 percent to more than 80 percent. However, these estimates did not include uncertainties in all components that contribute to the gravity field. In this study, we develop a forward model for the gravity anomaly. We combine density anomalies, isostatic balance, and non-isostatic contributions from GIA and dynamic topography. The largest uncertainty in the predicted gravity anomaly is due to the lower mantle viscosity; uncertainties in the ice history, the crustal model, the lithosphere-asthenosphere boundary and the conversion from seismic velocities to density are found to have a smaller effect. A preference for lower mantle viscosities $> 10^{22}$ Pa s is found, in which case at least 60 percent of the observed long-wavelength gravity anomaly can be attributed to GIA. This lower bound on the lower mantle viscosity has implications for models employing a viscosity profile in the mantle, such as models for mantle convection and GIA, and inferences based on these models.

Plain Language Summary

About 26 thousand years ago, vast parts of North America and Northern Europe were covered by ice sheets. These glaciations depressed the ground, which is rebounding ever since the ice sheets started melting. The rate of this rebound depends on the structure of the earth below it. In this paper, we obtain more insight into the structure of the earth. To do so, we use the gravitational field, since we can observe small deviations in this field very precisely. Over Hudson Bay, we observe such a deviation. The observed gravity anomaly over Hudson Bay closely resembles the area previously covered by ice. One possible explanation for this anomaly is therefore the incomplete rebound of the land. To test this, we include the effects of previous glaciations and mantle flow in a model of the crust and the lithosphere. We vary the viscosities of the upper and lower mantle, which are important parameters when modelling glacial rebound and mantle flow. The best match is found for a stiff lower mantle, implying that at least 200 meters of land uplift remains and that a minimum of 60 percent of this anomaly can be attributed to the depression caused by past glaciations.

1 Introduction

The global gravity model XGM2016 exhibits a negative anomaly of about 50 mGal near Hudson Bay for wavelengths larger than 600 km (Figure 1) (Pail et al., 2018). The location of this anomaly correlates with the area depressed by the Laurentide ice sheet during the Last Glacial Maximum (LGM) (Dyke & Prest, 1987; Lambeck et al., 2014; Stokes, 2017). Hence, the anomaly is thought to be caused by the incomplete rebound following the deglaciation of the Laurentide ice sheet (Kaula, 1972; Walcott, 1973), a process known as glacial isostatic adjustment (GIA). Because of incomplete GIA, the topography is not in equilibrium, and this topographic deflection can be seen in the gravity field. If GIA were the only cause for the gravity anomaly, the observed gravity anomaly with its small error would form a useful constraint on GIA models. However, in general, the static gravity field contains contributions from the top layers of the Earth, the mantle, and GIA. Before using the gravity anomaly to constrain GIA these contributions need to be quantified. Therefore, they are briefly discussed in the following paragraphs.

The most important contributions from the top layers of the Earth to the gravity field are from the large radial variations in the density. A density jump marks the boundary between the crust and the mantle, the Moho. Knowledge of the geometry of this bound-

ary is therefore important for gravity modelling. A second important boundary is the lithosphere-asthenosphere boundary (LAB), which can be defined as a boundary separating the conductive and convective regimes (e.g., Eaton et al., 2009; Fischer et al., 2010; Sleep, 2005). This boundary is not characterised by a large jump in density, but determines where the mantle can start to flow to equalise the weight of the overlying material. The LAB is therefore an important boundary, and can be inferred from estimates of, among others, heat flow or seismic tomography (Afonso et al., 2019; Eaton et al., 2009). Beneath Hudson Bay, the lithosphere is cratonic and has a thickness of 150-200 km (Eaton & Darbyshire, 2010).

Another important factor determining the gravity field contribution of the top layers of the Earth is isostasy. Isostasy implies that the pressures at a certain depth are equal. For example, the crustal thickness, which delivers the buoyancy to maintain the topography, can be determined in the classical Airy isostasy theory (crustal isostasy, Watts, 2001). In other studies, isostasy is calculated based on a lithosphere floating on top of a homogeneous asthenosphere (lithospheric isostasy, Lachenbruch & Morgan, 1990). Both methods can be employed to investigate the sensitivity to the top layers of the Earth (Métivier et al., 2016). The isostatically compensated crust can still contribute around 100 mGal in amplitude for wavelengths larger than 200 km (Root et al., 2017).

Mantle contributions to the gravity field consist of (i) density anomalies in the mantle, (ii) dynamic topography (Hager et al., 1985) and (iii) topography of the Core-Mantle Boundary (CMB). (ii) and (iii) depend on the viscosity contrast between upper and lower mantle; a smaller contrast results in a larger signal. (i) and (ii) have opposite sign; a positive density anomaly drags the surface down, resulting in negative dynamic topography which compensates the positive gravity anomaly from the density anomalies. The lower boundary of the mantle marks the largest density contrast in the Earth, larger than the density contrast at the surface. For long wavelength features it is therefore important to include (iii). The long wavelength signal in the gravity field and the geoid can be matched well by mantle convection modelling using seismic tomography as input for the mantle density distribution (Hager et al., 1985). For North America, the main mantle signal that is expected is that of the subducted Farallon slab, although its geometry and subduction history are not well defined (Sigloch, 2011).

The GIA contribution to the gravity field is, to a large extent, dependent on the ice sheet history and on the viscosity of the Earth's mantle. The ice history controls the deflection that can be reached in an Earth in equilibrium. Viscosity controls how fast the equilibrium is reached. A large viscosity can lead to a smaller initial displacement and a smaller remaining displacement, but fast relaxation from a low viscosity mantle also leads to a smaller remaining displacement. Viscosity is therefore an important factor in GIA models in general, and controls the value of the static gravity field anomaly for a given ice sheet history.

Previous studies attribute different percentages of the free-air gravity anomaly to GIA. This discrepancy can to a large extent be explained by different assumptions of the underlying mantle viscosity, and whether GIA and dynamic topography, as well as crustal and mantle density variations are considered in the modelling or data correction. The first studies that try to explain the free-air gravity anomaly over Hudson Bay note that the free-air gravity anomaly can not be explained by GIA using a lower mantle viscosity of 10^{21} Pa s, and suggest by inference that the major contribution is that of mantle convection (Cathles, 1975; James, 1992; Peltier et al., 1992). Simons and Hager (1997) find that the GIA contribution is significant and that about 50 percent of the free-air gravity anomaly can be explained by GIA. In their study, they employ a lower mantle viscosity that is close to 10^{22} Pa s. Tamisiea et al. (2007) used time-variable gravity from the GRACE mission to isolate the GIA signal and found viscosities between 10^{21} and 10^{22} Pa s. Consequently, they attribute only 25-45 percent of the free-air gravity anomaly to GIA. Finally, Métivier et al. (2016) used existing viscosity profiles and combined a

lithospheric model with GIA and mantle modelling, and found values of at least 10^{22} Pa s. In their study, GIA contributes more than 80 percent. All in all, the contribution of GIA to the free-air gravity anomaly is still uncertain, with most recent estimates ranging from 25-45 percent (Tamisiea et al., 2007) to more than 80 percent (Métivier et al., 2016), with part of the spread explained by the unknown mantle viscosity.

The mantle viscosity is not well constrained and many studies have attemped to determine its value by employing constraints on mantle convection models (e.g., Soldati et al., 2009; Steinberger, 2007), GIA models (e.g., Paulson et al., 2007; Wu & Peltier, 1983) or a combination of both (Forte & Mitrovica, 1996; Mitrovica & Forte, 2004). Mantle convection studies that determine the viscosity are often global studies. These global inferences of the viscosity are not readily applicable to North America, since viscosity might vary laterally. GIA studies have been performed on both a global and regional scale, and generally use relative sea level (RSL) data and geodetic data to constrain the viscosity. No consensus has been reached on the value of the viscosity in the lower mantle over North America, with values ranging two orders of magnitude (10^{21}-10^{23} Pa s) (e.g., Métivier et al., 2016; Paulson et al., 2007).

Dynamic models (i.e. the mantle convection model and the GIA model) contain more uncertain parameters than the viscosity. One of these parameters is the ice history, which is especially sensitive at the margin of ice sheets (Mitrovica et al., 1994; Wu, 2006). However, the extent of the Laurentide ice sheet is relatively well known, in contrast to its thickness (Stokes, 2017). Uncertainty due to the ice history has been included in some previous studies of the static gravity field (James, 1992; Métivier et al., 2016), but not in all (Peltier et al., 1992; Tamisiea et al., 2007). For mantle convection modelling, density anomalies are needed, which are commonly derived from seismic velocity anomalies. The conversion factor between velocity anomalies and density anomalies can vary between 0.2 and 0.4 (Karato, 1993; Trampert et al., 2004), as determined by measurements and employed in convection models (Steinberger & Calderwood, 2006). This conversion factor can have a large influence on the resulting gravity, as it can amplify or minimize gravitational signals from the mantle. Métivier et al. (2016) assign a conversion factor to each viscosity layer in their mantle models, but do not show the sensitivity to this parameter.

Thus, not all uncertainty in dynamic models and other components has been considered simultaneously. Also the effect of forces from GIA and dynamic topography on the isostatic balance usually employed in gravity field studies is not included consistently. For this reason, previous constraints on the lower mantle viscosity could be biased. In this study, we fit the observed long wavelength gravity anomaly in Laurentia (Figure 1) with models for GIA and mantle convection, and realistic models for the crust-lithosphere-asthenosphere, and account for uncertainties in all components. In our approach we also apply isostatic balance of the top layers, but we include the contribution of dynamic models to the force balance.

Section 2 explains the approach used to construct the density model of the crust-lithosphere-asthenosphere and its conversion to static gravity anomalies. After that, we elaborate on the GIA and mantle convection models used and how they included in the isostatic balance of the crust-lithosphere-asthenosphere. Section 3 starts by investigating the uncertainty of the crustal and lithospheric model to the gravity field. Next, we show the GIA and mantle contributions to the gravity field as a function of the viscosity profile. After this, we discuss uncertainties due to the ice history and due to the conversion from seismic velocities to density. We find the best fitting solution for an earth model with varying upper- and lower mantle viscosity, and obtain a lower bound on the lower mantle viscosity.

2 Methodology

In this section, we start by stating the complete model used in this study. The top layers are the crust, lithosphere and asthenosphere. Second, we explain how GIA and dynamic topography are incorporated in our crust-lithosphere-asthenosphere model using isostatic equilibrium. After that, we elaborate on the crust-lithosphere-asthenosphere models, the mantle models, and the GIA models. Finally, we determine the maximum spherical harmonic degree that we use in our analysis.

2.1 The complete model

Our forward model includes the gravity effect (Δg) of a crust-lithosphere-asthenosphere model (CLA), mantle density anomalies below 300 km (ρ_m), and topography at the CMB needs to be computed in order to obtain a reasonable comparison with the observed gravity field:

$$\Delta g_{tot} = \Delta g_{CLA} + \Delta g_{\rho m} + \Delta g_{CMB} \tag{1}$$

The non isostatic pressures of dynamic topography and GIA are included in the isostatic balance of the crust-lithosphere-asthenosphere model (Section 2.2). The gravity signal from mantle anomalies and the topography at the CMB are computed by a mantle convection model (Tosi, 2008).

For the crust-lithosphere-asthenosphere model, the gravity anomaly of the density layers needs to be computed. To do this, we use a spectral method that transforms 3D spherical density models into spherical harmonic coefficients (Root et al., 2016), and use the SHTools package (Wieczorek & Meschede, 2018) to synthesise the coefficients to gravitational potential fields. Although the geoid is commonly used, we opt to show gravity disturbance, which is the radial derivative of the gravity potential. Our choice to represent the gravity field is in principle arbitrary for the long-wavelengths that we employ in this study. Strictly speaking, we are computing gravity disturbances, these disturbances are referred to as gravity anomalies in this study.

2.2 Isostasy in the Crust-Lithosphere-Asthenosphere model

In principle, the gravity field can be represented by geometry and density information of each layer in the sub-surface. In practice, accurate density information is not available at each depth, and the assumption of isostasy is made to solve for densities or geometry. In this study, we employ lithospheric isostasy (Lachenbruch & Morgan, 1990; Root et al., 2017), which involves adjusting the density of the lithosphere.

To implement lithospheric isostasy, free body diagrams are made of mass columns up to 300 km (Figure 2). The forces involved are those caused by the weight of the crust, lithospheric mantle, and asthenosphere, and we implement GIA and dynamic topography as pressure forces acting at 300 km. The pressure at 300 km depth for each column should equal that exerted by a reference column. Here, the reference column consists of a 30 km thick crustal layer and a 270 km thick mantle layer with densities of 2850 kg/m^3 and 3300 kg/m^3, respectively (Figure 2). Equilibrium of the forces is then achieved in the following manner:

$$F_{crust} + F_{litho} + F_{asth} - F_{GIA} - F_{dt} = F_{reaction} = F_{ref} \tag{2}$$

For each layer the pressure at 300 km can simply be calculated from its weight per area. To include dynamic topography, we transform the stress caused by this process into an equivalent hydrostatic pressure (Flament et al., 2013):

$$\sigma_{rr} = \rho_{asth} g h_{dt}, \tag{3}$$

where the density (ρ_{asth}) is that of the asthenosphere and equal to 3300 kg/m^3, g is the average value of the gravity, and h_{dt} is the height of the dynamic topography. σ_{rr} is calculated by the mantle convection model (Tosi, 2008), discussed in Section 2.4.

In principle, the contribution of GIA above 300 km is already included in the geometry of the crust and lithosphere, because their boundaries are deflected by GIA. However, this signal is small compared to the uncertainty in the geometry of the crust and lithosphere. Because our goal is to generate a complete gravity field model, both GIA and dynamic topography need to be included in the isostatic balance. It is important to not correct with a full GIA model when the observed geometry of the crust and upper mantle is used in a forward model. Following the approach of Root et al. (2015), we implement the effect of GIA by shifting the layers above 300 km according to the respective GIA deflection at that point, h_{GIA}, defined positive downwards. This way, we assume isostasy based on a configuration in which GIA is no longer present. h_{GIA} is calculated by the GIA model, discussed in Section 2.5.

Combining these ideas in the force balance (Equation 2), assuming constant gravity in the top 300 km yields:

$$\begin{aligned} \textstyle\sum_i \int_{Moho+h_{GIA}}^{topo+h_{GIA}} \rho_{crust,i} dV + \int_{LAB+h_{GIA}}^{Moho+h_{GIA}} \rho_{litho} dV + \int_{LAB+h_{GIA}}^{Moho+h_{GIA}} \Delta\rho dV \\ + \int_{300km}^{LAB+h_{GIA}} \rho_{asth} dV - \int_{0}^{dyn.topo} \rho_{asth} dV = \int_{300km}^{0} \rho_{ref} dV \end{aligned} \tag{4}$$

An earlier version of this equation, without the processes of GIA and dynamic topography, is shown in Root et al. (2017). The first, second, and fourth term on the left-hand side of the equation represent the masses of all the crustal, lithospheric, and asthenospheric layers in the model, respectively, and the right-hand side represents the mass of the reference column. The radii to the Moho and the topographic boundaries are defined positive upwards. We assume that the geometry and density of the crust are reasonably well known from seismic data compared to deeper layers. Therefore, we opt to adjust the density of the mantle lithosphere, which is less well known, and is represented by the third term in equation 4. It is important to note that the GIA contribution to the first four terms contains the entire GIA contribution (Root et al., 2015). Boundaries below 300 km have a smaller density change and/or a smaller deflection and these are neglected. Similarly, the fifth term contains all of the effect of dynamic topography. This term is negative, because σ_{rr} is defined positive upwards in equation 3, and, consequently, the direction of this load is opposite that of the gravitational loads. Thus, a positive dynamic topography contribution results in an effective negative mass that will be compensated because of the pressure balance represented by Equation 4.

To recapitulate, the force balance (Equation 2) is transformed into a pressure balance. We can do so, because the area of the model columns is the same as that of the reference column. From the pressure balance, we assume that the equivalent hydrostatic pressures of all the mass layers can be calculated using Equation 3 with the corresponding densities. Assuming that gravity is constant for all layers in the crust-lithosphere-asthenosphere model, we obtain the mass balance shown in Equation 4.

2.3 Crust, Lithosphere, and Asthenosphere Models

To account for uncertainty in the crustal thickness, two crustal models are used: CRUST1.0 (Laske et al., 2013) and a crustal model based on the U.S. Geological Survey (USGS) Global Seismic Catalog (GSC) database, which was interpolated to a 1x1°

grid using kriging interpolation (Szwillus et al., 2019). This dataset has been augmented over North America with data from the Geological Survey of Canada (Schetselaar & Snyder, 2017), and will be named GSCaug hereafter. CRUST1.0 has a resolution of 1x1° and each cell has a unique 8 layer density profile profile. The GSCaug dataset only presents the Moho depth. We adopt a crustal density of 2850 kg/m^3 for the GSCaug dataset, based on the reference profile described in section 2.2. For both crustal models, the topography, bathymetry and ice-cover are taken from CRUST1.0, as uncertainties in these components are negligible for the long wavelength signal studied in this article. Moho depths of the crustal models are shown in Figure 4a and 4b. In oceanic areas, the Moho depth is 20 km at most. The Moho depth is clearly larger for continental areas, with values of 30 to 50 km. Around Hudson Bay, there are regional differences of up to 10 km between the crustal models. CRUST1.0 is used as the default crustal model in the rest of the analysis. This is different from Métivier et al. (2016), in which an isopycnal configuration of the crust was used.

The lithosphere and the asthenosphere are separated by the LAB. To account for uncertainty in this depth we use two estimates for the LAB (Figure 4c and 4d). The first option is the LAB model of Hamza and Vieira (2012) and the second option is obtained from WINTERC v5.2, which is a 3D model of the lithosphere and the upper mantle based on a joint-inversion of surface wave form tomography, surface heat flow, and elevation of the topography. Within WINTERC v5.2, mantle densties and seismic velocities are computed within a self-consistent thermodynamic framework as a function of pressure, temperature and bulk composition. In both models, the LAB reaches its largest depth in an area below Hudson Bay, thereby correlating with the observed gravity anomaly. In the LAB model compiled by Hamza and Vieira (2012), the LAB low over Hudson Bay is more confined and larger in amplitude than the WINTERC LAB.

We have used the LAB from Hamza and Vieira (2012) as our reference model, and the LAB estimate from WINTERC v5.2 as our alternative model, in the remainder of this study. However, the LAB from Hamza and Vieira (2012) is probably not well constrained, since it is derived from estimates of surface heat fluxes. These estimates form a poor constraint in terms of sparsity and error. However, since there is no real density jump at the LAB, we do not expect large changes in the gravity field as a result of the choice here.

As mentioned in Section 2.2, the lithospheric mantle densities are adjusted to ensure isostasy. We assign a single lithospheric density to each grid cell between the Moho and the LAB. We obtain lithospheric densities between 3320 and 3380 kg/m^3 (Fig A1a) using the LAB from Hamza and Vieira (2012). The range in lithospheric densities is larger (3140 - 3500 kg/m^3) for the WINTERC v5.2 LAB (Fig A1b). The largest differences between the modelled densities are present in areas where the lithosphere is relatively thin, since here the densities need to be adjusted more to accomodate a similar change in LAB. In areas where the lithosphere is thick, like Hudson Bay, differences in the modelled lithospheric densities are less prominent. Thus, because the LAB is used to determine the lithospheric density needed for isostasy, the sensitivity of the gravity anomaly to the LAB estimate is reduced. The sensitivity to this choice is investigated more thoroughly in Section 3.

2.4 Mantle below 300 km

The contributions of the mantle below 300 km are computed using a mantle convection model (Tosi, 2008). This spectral finite element code solves the incompressible Stokes problem and computes the geopotential field resulting from density anomalies and boundary deflections. For the radial direction, the model employs finite elements, while for the angular direction spherical harmonics are used to parameterise the solutions to

the Stokes problem. The model uses mantle density anomalies as input, and produces dynamic topography at the surface (Hager et al., 1985) and at the CMB.

The density anomalies are in turn derived from seismic velocity anomalies. Here, the seismic velocity anomalies are taken from the global, composite tomography model SMEAN2 (Becker & Boschi, 2002), which incorporates S40RTS (Ritsema et al., 2011), GyPSUM-S (Simmons et al., 2010) and SAVANI (Auer et al., 2014). Shear-wave velocity anomalies (Δv) can be converted to density anomalies ($\Delta \rho$) by a conversion factor (p) (Karato, 2008):

$$\frac{\Delta \rho}{\rho} = p \frac{\Delta v}{v}. \tag{5}$$

In this study, the conversion factor has a constant value of 0.15. In reality, the conversion factor can change radially (Karato, 2008; Steinberger & Calderwood, 2006), but a single value is sufficient if the sensitivity to the parameter is small. The uncertainty introduced by the conversion factor is analysed in section 3. The converted density anomalies, together with a three-layered viscosity profile (elastic lithosphere, upper mantle, and lower mantle), are used as input in the mantle convection code. The lithosphere is assumed to have a thickness of 100 km. The viscosities of the upper and lower mantle are separated by the 670 km discontinuity. The density of the core is assumed to be homogeneous and is set equal to 4500 kg/m^3. The CMB and the Earth's surface are modelled as free-slip, impermeable boundaries. The output of the mantle convection code consists of stresses at the top and bottom boundaries. The stresses are converted to dynamic topography values with Equation 3. After, the surface dynamic topography is converted to pressure to compute lithospheric density anomalies to fulfil isostatic balance in the crust-lithosphere-asthenosphere model using Equation 4. The mantle density anomalies and the CMB topography are converted to spherical harmonic coefficients following the approach of Root et al. (2017), and these coefficients are added to the coefficients from the crust-lithosphere-asthenosphere model to complete the total gravity signal as in Equation 1, such that it can be compared to gravity field observations.

2.5 GIA models

The GIA response to the glacial loading is calculated with a normal mode method (Wu & Peltier, 1982) for a multilayer model (Vermeersen & Sabadini, 1997) with self-consistent sea levels (Mitrovica & Peltier, 1991b). Rotational feedback (Milne & Mitrovica, 1998; Wu & Peltier, 1984) and geocenter motion (Greff-Lefftz & Legros, 1997) are both incorporated in the model. The code is developed by Schotman (2008) and has recently been benchmarked for simple loading scenarios in Martinec et al. (2018). GIA models with a 1D viscosity in North America match results from 3D models, from which the 1D viscosity was obtained by averaging, reasonably well (A et al., 2013), and the effect of 3D viscosity on predictions around Hudson Bay is limited (Li et al., 2020). Therefore, it is expected that the 1D Earth model produces reasonably accurate results.

The GIA model adopts a similar 3-layer Earth model as the mantle convection code discussed in Section 2.4, consisting of an 80 km thick, elastic lithosphere and a viscous upper (<670 km) and lower (>670 km) mantle. The elastic parameters are obtained from the Preliminary Reference Earth Model (PREM; Dziewonski & Anderson, 1981) and are the same as in van der Wal et al. (2009). This lithospheric thickness is different than that of the mantle convection model, but since our results turned out to be insensitive to the lithospheric thickness (Figure B1), this difference will not have a large effect.

An important uncertainty in the GIA model is caused by the unknown ice loading history. Four different ice histories are employed to assess this uncertainty. The ice models are: ICE-6G (Argus et al., 2014; Peltier et al., 2015), the model by Lambeck et

al. (2017), which will be labelled LW-6, and two variants of the GLAC-1D model (Tarasov et al., 2012), named GLAC-1D nn9894 and GLAC-1D nn9927. The ICE-6G and GLAC-1D models are global models, while LW-6 is a regional model. ICE-6G uses ice extent constraints and is tuned to fit relative sea level (RSL) data and geodetic constraints, although the fitting started with a model based on ice dynamics. The North American sector of GLAC1-D uses much of the same RSL and geodetic constraints as that of ICE-6G, as well as marine limit and strandline data. It also accounts for age uncertainty in the geologically-inferred deglacial margins and is derived from an approximate Bayesian formalism applied to a thermo-mechanically coupled glaciological model. Each of the models require an implicit viscosity profile, but the bias introduced by the viscosity is smallest for the GLAC-1D models that are primarily controlled by ice dynamics. The ICE-6G and GLAC-1D models are based on the VM5a viscosity profile (Peltier et al., 2015), while the viscosity profile used for the LW-6 model consists of a three layer viscosity profile with an upper mantle viscosity of 5.1×10^{20} Pa s and a lower mantle viscosity of 1.3×10^{22} Pa s. Ice thicknesses at 26 ka are up to 5000 meter in the ICE-6G model, and up to 4000 meter in the other models (Figure 5). ICE-6G also has thicker ice in the western part of North America compared to the other models. Together, this is a partial representation of the uncertainty in the ice loading history. For all models, three glacial cycles are used, up to 224 ka, to account for the effect on the gravity anomaly of earlier glaciations in models containing larger values for the lower mantle viscosity. The first two glacial cycles are assumed to be the same as the last one.

2.6 Spherical Harmonic Truncation Limit

The signal that we want to explain is the long-wavelength gravity field, which contains most of the GIA and mantle convection. The truncation limit should be a trade-off between containing most of the GIA and mantle signal, and minimizing the uncertainties in the other components, especially in the crustal model, which can introduce uncertainties up to 110 mGal (Root et al., 2015). Also, the lithospheric density anomalies are especially uncertain in the short-wavelength region. Another argument in favor of a low maximum Spherical Harmonic (SH) degree is the assumption of local isostasy made in the model, which works best for long wavelength signals (Gvirtzman et al., 2016; Watts, 2001), since flexural isostasy starts to contribute significantly to degrees larger than ~ 30 (Watts & Moore, 2017).

Mantle convection manifests itself in longer wavelengths, and contains most of its signal below SH degree 10 (e.g., Gu et al., 2001; Steinberger et al., 2019; Su & Dziewonski, 1991). Therefore, the truncation is mostly determined by the GIA signal. In Figure 3, the amplitude and the location of the GIA signal are plotted for models containing an upper mantle viscosity of either 2×10^{20} or 4×10^{20} Pa s and a lower mantle viscosity $>10^{21}$ Pa s. The solid lines result from models with an upper mantle viscosity of 4×10^{20} Pa s and a lower mantle viscosity of 3.2×10^{21} Pa s (blue), 1.3×10^{22} Pa s (green) and 2.6×10^{22} Pa s (red). The gravity anomaly for different viscosity profiles is represented by the shaded areas and exhibits the same behaviour as shown by the solid lines.

The idea is to find a truncation limit above which the GIA gravity signal loss is relatively small. The amplitude of the GIA signal over North America starts to decrease for a maximum SH degree lower than 20, stabilises again and then decreases rapidly for a maximum SH degree lower than 10 (Figure 3a.). A second criterion is based on the location of the maximum amplitude of the GIA signal in the models. For different truncation limits, the location of the maximum amplitude in the gravity field is compared to that of the original model, which uses a maximum SH degree of 50 (Figure 3b.). This distance starts to increase significantly for truncation limits smaller than 20. For a truncation limit at SH degree 10, the distance to the original maximum amplitude is almost 300 km. Since the uncertainty in the crustal signal is especially small for a maximum

SH degree of 15 or less, we will use SH degree 15 as the maximum degree for all models and observations in the rest of this study.

3 Results

Figure 6a shows the gravitational signal due to a combination of our crustal model (CRUST1.0) and our LAB (taken from Hamza & Vieira, 2012). A small gravity low of up to 15 mGal is present just Southwest of Hudson Bay. This gravity anomaly extends to the south and reaches 30 mGal south of Lake Michigan. The gravity high over the Rocky Mountains is up to 20 mGal. The uncertainty due to the crust can be caused by: i) the density profile adopted, and ii) the Moho employed in our model. To determine the effect of uncertainty in the density profile, we compare the gravitational signal from a layered density profile with that of an isopycnal crust with a density of 2850 kg/m^3, without changing the Moho (in both cases, the Moho is that of CRUST1.0). The fact that we only focus on spherical harmonic degrees 2 to 15 greatly reduces the uncertainty, as only the long wavelength signals remain, and these are generally more consistent among different crustal models (Figure 6b-e). Uncertainty over Hudson Bay is small and for the most part below 5 mGal. In two regions, uncertainty reaches 10 mGal, namely in the Canadian Arctic Archipelago and in the geologically complex Rocky Mountains. Figure 6c shows the uncertainty due to the Moho. This is the spread in gravity signal caused by employing the CRUST1.0 and the GSCaug Moho models. When determining the Moho uncertainty, we have made use of an isopycnal crust. Uncertainties due to the Moho are small and, with the exception of the region over the Canadian Arctic Archipelago, below 5 mGal. We determine the LAB uncertainty in the same way as the Moho uncertainty. Uncertainty in the gravity contribution due to different LAB representations is only up to 5 mGal over Hudson Bay (Figure 6d). The reasons for these small numbers, despite large differences in LAB, are the compensating effect of fitting lithosphere densities to the isostasy constraint and the absence of a density jump at the LAB. In total, uncertainties due to the crustal model and the LAB add up to 15 mGal in the south and only 10 mGal around Hudson Bay (Figure 6e).

GIA and dynamic topography both contribute to the total modelled gravity signal of the crust-lithosphere-asthenosphere model. To compare the contributions of GIA and the mantle, the GIA and dynamic topography heights calculated in Section 2 are converted to SH coefficients. The SH coefficients from mantle density anomalies and CMB topography are added to that of dynamic topography to form the total effect of the mantle. From the SH coefficients for GIA and the mantle, the gravity anomalies can be calculated and compared. We vary the viscosity values of the upper and lower mantle between 10^{20} and 10^{23} Pa s and calculate the gravity signal at the location of the minimum in the gravity anomaly. Figure 7 exhibits a wide range of values, depending on the viscosity profile. The GIA contribution is most sensitive to the viscosity of the lower mantle. For lower mantle viscosities $>10^{22}$ Pa s, GIA contributes at least 30 mGal to the negative anomaly. This contribution decreases when the lower mantle viscosity decreases. Lower viscosities imply a shorter relaxation time, and consequently less remaining uplift is present in the lithosphere. This results in a smaller contribution to the static gravity field. For all viscosity profiles, the contribution of the mantle below 300 km does not exceed -20 mGal, and can even be weakly positive for lower mantle viscosities $>10^{22}$ Pa s. The crust and lithosphere contributions do not depend on the underlying viscosity profile, and contribute 15 $\pm$ 10 mGal to the gravity anomaly (Figure 6a).

Since our results are most sensitive to the lower mantle viscosity, we look for constraints on this parameter, taking into account uncertainties in other components. In order to place constraints on the viscosity of the lower mantle, we have created models according to Equation 1 for different combinations of the upper and lower mantle viscosity and compared these with the observed static gravity field. We have done this for the area depicted by the red dashed line in Figure 1, which is the area covering Hudson Bay

and the region south of Hudson Bay up to major lakes like Lake Michigan. A misfit is then calculated using the following formula:

$$\chi^2 = \frac{1}{N} \sum_{i=1}^{N} \left(\frac{o_i - p_i}{\sigma_i} \right)^2 , \tag{6}$$

where N is the number of gridpoints, and o_i and p_i are the observations and the predicted values at gridpoint i, respectively. σ_i is the uncertainty, which is determined from the spread in the gravity field due the crustal and lithospheric model at that specific point (Figure 6e). The spread in the signal due to the crust-lithosphere-asthenosphere model is independent of the underlying viscosity and can be seen as way to represent uncertainty in the final signal. The misfit for different upper and lower mantle viscosities is shown in Figure 8. Since the values of the observed gravity anomaly at each gridpoint are correlated, we can not attribute confidence intervals. Instead, χ^2 values less than 6.25 are denoted by circles, to highlight the better performing models which fit the data on average within 2.5σ. The well performing models are found almost exclusively for lower mantle viscosities of more than 10^{22} Pa s (Figure 8). Models containing lower mantle viscosities in the range 10^{21} - 10^{22} Pa s underestimate the negative anomaly in the gravity field observed over Hudson Bay, naturally resulting in high χ^2 values. The good fit for lower mantle viscosities above 10^{22} Pa s does not change if we change the lithospheric thickness in the GIA model from 80 km to 115 km or to 150 km (Figure B1), or if we define the area of interest to contain all points that have a value that is at least 40 percent of the peak value, as opposed to the 50 percent threshold used in the rest of this study. Moreover, if simulations were performed with a different spherical harmonic truncation limit (e.g., 14 or 16 as the upper limit), the general patterns in the misfit plot remain the same. The most important other sources of uncertainty are discussed in the following paragraphs.

The next parameter that we will discuss is the ice history, which is used as an input to the GIA model. Variations in ice heights and the time of melting translate directly in the gravity signal (Mitrovica & Peltier, 1991a). The subplots in Figure 8 correspond to the four ice histories used. Lower mantle viscosities $>10^{22}$ Pa s show lower misfit values, regardless of the ice model used. This confirms that the preferred viscosity profile does not depend strongly on the ice history. For the GLAC-1D nn9894 ice history, lower mantle viscosities of 6.4×10^{21} Pa s also perform well. However, for these specific well performing models, the upper mantle viscosity needs to be $>10^{21}$ Pa s, which is not corroborated by other studies on the viscosity of the upper mantle in North America (e.g., Paulson et al., 2007; Sasgen et al., 2012; Tamisiea et al., 2007; Wolf et al., 2006). Thus, regardless of the employed ice history, lower mantle viscosities $>10^{22}$ Pa s are preferred.

The final parameter that we will test the sensitivity to is the conversion factor from seismic velocity anomalies to density anomalies. We vary the conversion factor between 0.1 and 0.4 to represent the range of possible values (Trampert et al., 2004) and study its effect on our conclusions. For each conversion factor a χ^2 misfit is calculated using Equation 6. The largest sensitivity is to the viscosity of the lower mantle. For this reason, Figure 9 shows the spread in χ^2 values as a function of the lower mantle viscosity, while the upper mantle viscosity is kept fixed at 4×10^{20} Pa s. Almost all models containing lower mantle viscosities $>10^{22}$ Pa s have a lower χ^2 value than models containing lower mantle viscosities $<10^{22}$ Pa s, independent of the conversion factor used. The spread in misfit values between observations and models decreases when the lower mantle viscosity is increased. This is because, for those viscosities, the contribution of the mantle convection signal is close to zero, or just about positive over North America (see Figure 7). Consequently, an amplification or reduction does not alter this contribution much. Hence, the preferred viscosity profile is not sensitive to the conversion factor, in

agreement with findings by King (1995), justifying our choice for a single value of the conversion factor of 0.15.

Figure 10 shows the residual between the model with the lowest χ^2 value and the gravity observations. We find the lowest misfit for the LW-6 ice history, using an upper mantle viscosity of 4×10^{20} Pa s and a lower mantle viscosity of 2.56×10^{22} Pa s. Some residuals can be expected over other areas over North America, as the misfit is only calculated over Hudson Bay. Nevertheless, the negative residual to the southwest of Hudson Bay near the Rocky Mountains deserves special attention, because it influences the gravity anomaly inside the region bounded by the contour in Figure 1. There are several possible explanations for this anomaly: Figure 6b suggests that the uncertainty in the density profile is the cause, as a clear uncertainty over the Rocky Mountains due to the density profile is exhibited. Employing an isopycnal crust indeed improves the fit, but does not enable the full removal of the anomaly over the Rocky mountains. Other options are changes in the LAB (see Figure 6d) or the effect of lateral viscosity changes in GIA models(e.g., A et al., 2013; Kuchar et al., 2019; Paulson et al., 2005).

4 Conclusion & Discussion

In this study, we combined dynamic models for GIA and mantle convection with a crust-lithosphere-asthenosphere model, and matched the results to the long-wavelength static gravity anomaly. The dynamic pressures caused by GIA and dynamic topography are implemented in the crust-lithosphere-asthenosphere model to compute the lithospheric density anomalies that are needed for isostasy. We argue that this is a necessary step to be able to derive a consistent forward gravity field model. Uncertainties in the ice history, crustal model, LAB and conversion factor are found to be small enough in the long-wavelength domain, such that a lower bound can be placed on the lower mantle viscosity. The best fitting model to the gravity field observations is found when lower mantle viscosities are larger than 10^{22} Pa s. Our results do not constrain the upper mantle viscosity, as the better performing models are present for the full range of upper mantle viscosities (10^{20} - 10^{21} Pa s) preferred in previous studies (e.g., Paulson et al., 2007; Sasgen et al., 2012; Tamisiea et al., 2007; Wolf et al., 2006).

Previous studies have suggested that the gravity anomaly over Hudson Bay is mainly due to mantle convection (Cathles, 1975; James, 1992; Peltier et al., 1992). Peltier et al. (1992) found that conversion factors (from seismic velocities to densities) in the range of 0.5-1.5 are needed to explain the gravity anomaly by mantle convection, which is large compared to recent estimates which are in the range 0.1-0.4 (Trampert et al., 2004). Tamisiea et al. (2007) attributed less than 50 percent (25-45%) of the anomaly to GIA. They estimated the viscosity based on gravity rates, but did not check whether the remaining percentage can be explained by mantle convection and did not include crustal and lithospheric density anomalies. Our results show that at least 60 percent of the negative anomaly in the static gravity field can be attributed to GIA, which agrees with previous studies that also found a preference for a lower mantle viscosity $> 10^{22}$ Pa s (Métivier et al., 2016; Simons & Hager, 1997).

Earlier GIA studies found that two sets of viscosity profiles result in small misfit values, which is classical for GIA models (Caron et al., 2017; Nakada & Okuno, 2016). The first set of well-performing models contains lower mantle viscosities between 10^{21} and 10^{22} Pa s, whereas the second set has lower mantle viscosities greater than 10^{22} Pa s. Solutions containing lower mantle viscosities between 10^{21} and 10^{22} are derived from data on: RSL (Cianetti et al., 2002), GRACE gravity rates (Tamisiea et al., 2007; van der Wal et al., 2008), GPS (van der Wal et al., 2009) or a combination of two of these (Paulson et al., 2007; Zhao, 2013). ICE-6G is based on the VM5a viscosity structure, which has a lower mantle viscosity $<10^{22}$ Pa s (Peltier & Drummond, 2008).

In contrast, several studies have found a high viscosity in the lower mantle, for example by an inversion of GPS, tide level gauges, absolute gravimetry and sea level indicators (Wolf et al., 2006) or by inverting for gravity rate observations from GRACE together with present-day ice mass changes in Alaska and Greenland (Sasgen et al., 2012). Root et al. (2015) showed a bifurcation among viscosity models for Fennoscandia, also favouring higher viscosity values. Steffen et al. (2009) compared GRACE solutions with results of a GIA model adjusted to fit RSL curves and found 2×10^{22} Pa s for the lower mantle viscosity. Geological evidence for RSL change and the tilting of paleo lake shorelines, combined with present-day crustal movement converged to high lower mantle viscosity models (Lambeck et al., 2017). Métivier et al. (2016) used gravity gradients and concluded that lower mantle viscosities larger than 2×10^{22} Pa s are preferred. This agrees with analysis of $\dot{J}_2$ data, which required viscosities above 5×10^{22} Pa s in the lower part of the lower mantle (Nakada & Okuno, 2016). Finally, Kuchar et al. (2019) found that an average viscosity of 3×10^{22} Pa s is needed to fit RSL data in 1D models and that the evolution of the peripheral bulge near the Atlantic and Gulf coast is what requires these high viscosities. While the area investigated here does not include the peripheral bulge near the Atlantic and Gulf coast, results from our model, constrained by the static gravity field, exhibit a clear preference for lower mantle viscosities $> 10^{22}$ Pa s The lower mantle viscosity affects inferences based on GIA models, such as the distribution of ice volume required to close the sea level budget at LGM (Lambeck et al., 2014).

In general, mantle convection studies are global studies, employing a more complex viscosity profile than used in our study. Nevertheless, the viscosity found in our study is in rough agreement with studies on slab sinking speeds (Čížková et al., 2012), mantle convection (e.g., Bower et al., 2013; Perry et al., 2003; Steinberger, 2007), or when mantle convection is combined with GIA (Mitrovica & Forte, 2004). In three-layered mantle convection models, one of the important parameters determining the amplitude and shape of the dynamic topography is the increase in viscosity between the upper and lower mantle. Since the upper mantle viscosity over North America is found to lie between 10^{20} and 10^{21} Pa s (e.g., Paulson et al., 2007; Sasgen et al., 2012; Tamisiea et al., 2007; Wolf et al., 2006), lower mantle viscosities $> 10^{22}$ Pa s require a jump that is likely to be at least a factor of 20 at the boundary between the upper and lower mantle. This is consistent with other mantle convection studies (Rudolph et al., 2015), but deviates somewhat from a study that found a jump of only 10 between the upper and lower mantle viscosity (Liu & Zhong, 2016). All in all, our results are not in conflict with most studies on mantle convection and supports a larger contrast between the upper and lower mantle viscosity, which favours slower slab sinking speeds (Van der Meer et al., 2018).

We have developed an approach to combine crust-lithosphere-asthenosphere models with models for GIA and dynamic topography consistently using isostasy. Our approach can in principle be applied to other regions that experience ongoing large scale GIA, like Fennoscandia, Alaska, and Antarctica. The spherical harmonics were truncated at degree 15, which diminished uncertainties due to the crustal model that were previously found to be large in Scandinavia (Root et al., 2015). If we studied small scale GIA signals, a larger uncertainty would be introduced by the crustal model. Since mantle convection covers the long wavelengths, this concept could also be useful for regional mantle convection models that aim to constrain viscosity or the conversion factor from seismic velocities to densities.

Appendix A Isostatic lithospheric mantle densities

Lithospheric mantle densities are adjusted to fulfil the requirement of isostasy. The adjusted lithospheric mantle densities are shown in Figure A1. The range in values for the lithospheric mantle density is larger when the WINTERC 5.2 LAB is used, compared to that using the LAB from Hamza and Vieira (2012). This implies that larger lateral

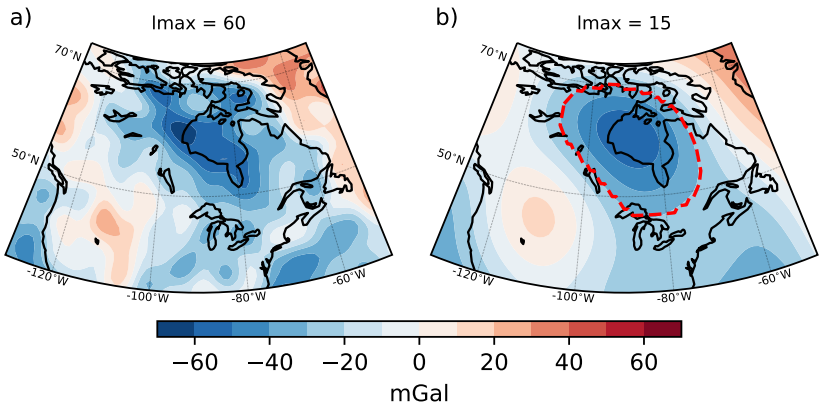

Figure 1. The static gravity field of XGM2016 (Pail et al., 2018) over North America up to degree 60 (a) and up to degree 15 (b). The study area is indicated by the dashed red line, which contains the points where the value is at least 50 percent of the peak value.

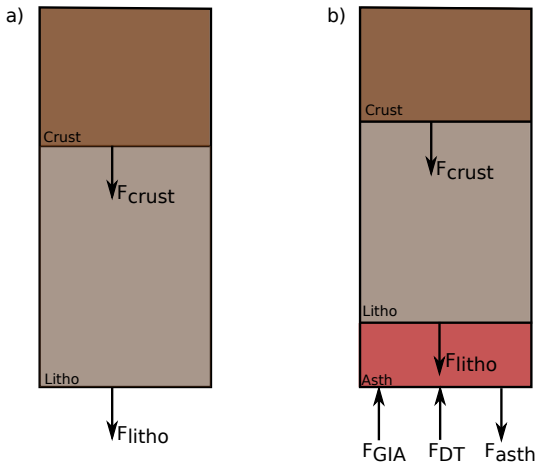

Figure 2. The forces involved in the reference column (left) and in our model (right). The forces exerted by the crustal, lithospheric and asthenospheric layers are denoted by F_{crust}, F_{litho} and F_{asth}, respectively. F_{GIA} and F_{DT} are the forces due to GIA and dynamic topography.

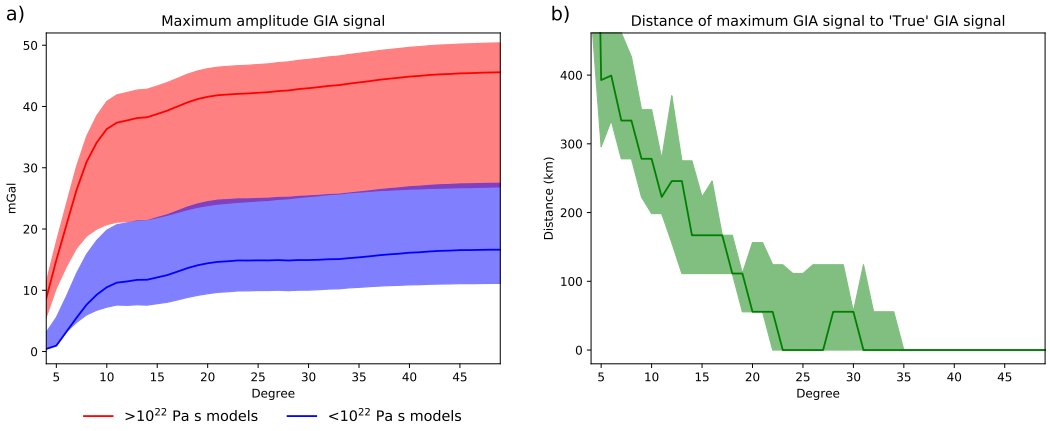

Figure 3. The amplitude of the GIA signal, according to the GIA models employed in this study (a) and the distance of the maximum GIA signal to the maximum GIA signal using spherical harmonic degree up to 50 (b). The red and blue lines represent the first ($10^{21} < \nu_{lm} < 10^{22}$ Pa s) and second ($\nu_{lm} > 10^{22}$ Pa s) set of models, respectively. The shading encompasses all models within each set. For b, results from the sets of models are indistinguishable and therefore shown together. The solid lines represent the result for $\nu_{um} = 4 \times 10^{20}$ (all solid lines) and $\nu_{lm} = 3.2 \times 10^{21}$ Pa s (blue), 1.3×10^{22} Pa s (green) and 2.6×10^{22} Pa s (red).

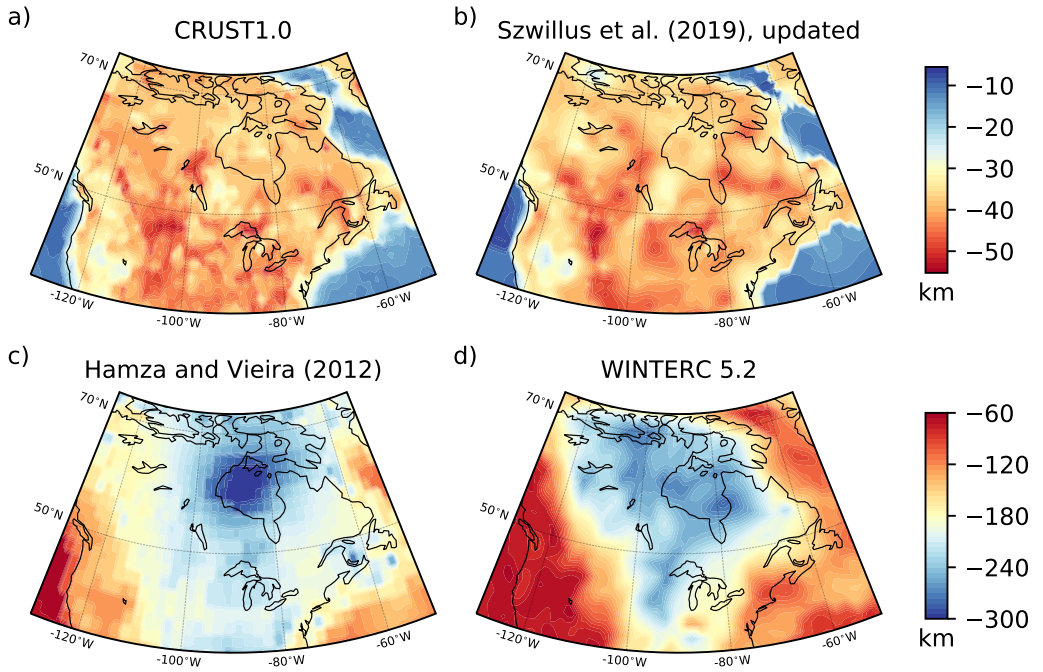

Figure 4. Moho depth of a) CRUST1.0 (Laske et al., 2013), and b) an augmented version of the Moho model compiled by Szwillus et al. (2019), as well as the LAB depth of c) Hamza and Vieira (2012), and d) WINTERC v5.2.

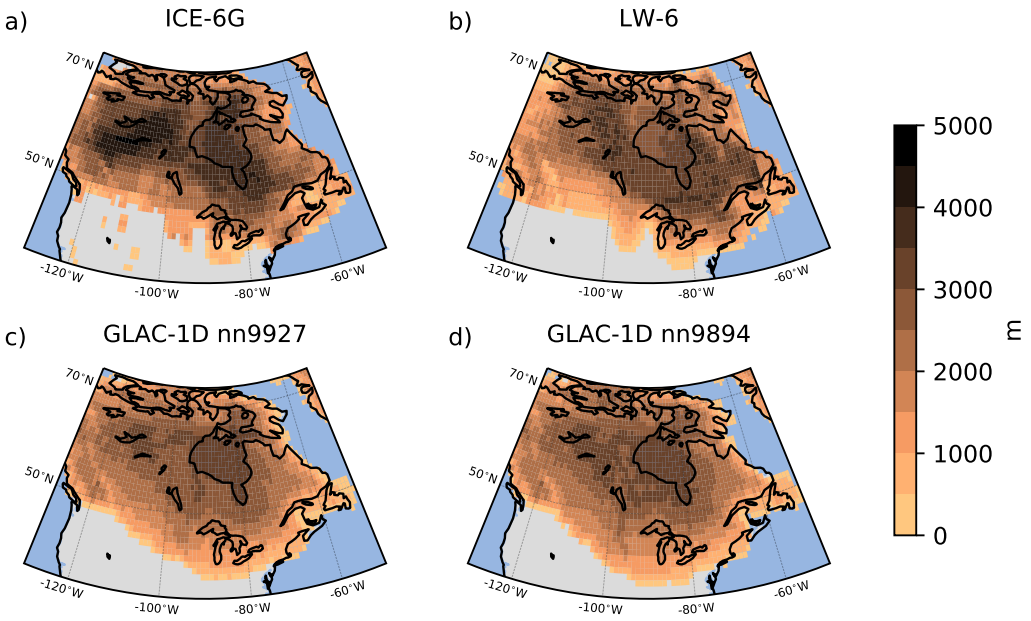

Figure 5. The ice thickness at LGM (26 ka) for the ice histories used in this study: a) ICE-6G (Peltier et al., 2015; Argus et al., 2014), b) LW-6 (Lambeck et al., 2017), and c-d) two GLAC-1D models (Tarasov et al., 2012)

changes in lithospheric mantle density are needed to satisfy the isostasy requirement when WINTERC 5.2 is used for the LAB.

Appendix B Lithospheric thickness variations

Another potentially important parameter is the thickness of the elastic lithosphere (e.g., Wang & Wu, 2006; Wu, 2005), used in the GIA model. Varying the lithospheric thickness from 80 km to 115 km or to 150 km does not alter the main conclusions of this study, as lower mantle viscosities $>10^{22}$ Pa s are preferred regardless of the lithospheric thickness employed (Figure B1).

Appendix C Contributions of GIA and mantle convection

As we have seen that the static gravity field can constrain the lower mantle viscosities, it is insightful to exhibit the seperate contributions of GIA and the mantle below 300 km, and its dependence on the lower mantle viscosity. Depending on the lower mantle viscosity, the GIA signal can be up to 20 mGal (Fig C1a) or up to 40 mGal (Fig C1b). For mantle convection, amplitudes are lower, but the sign can be reversed depending on the lower mantle viscosity. For a lower mantle viscosity of 3.2×10^{21} Pa s, the signal is weakly negative and consequently contributes positively to the observed static gravity anomaly (Fig C1c). For a viscosity of 2.6×10^{22} Pa s, anomalies due to mantle convection are weakly positive over Hudson Bay (Fig C1d). The positive signal in Figure C1d compensates slightly for the increased amplitude of the negative anomaly due to GIA.

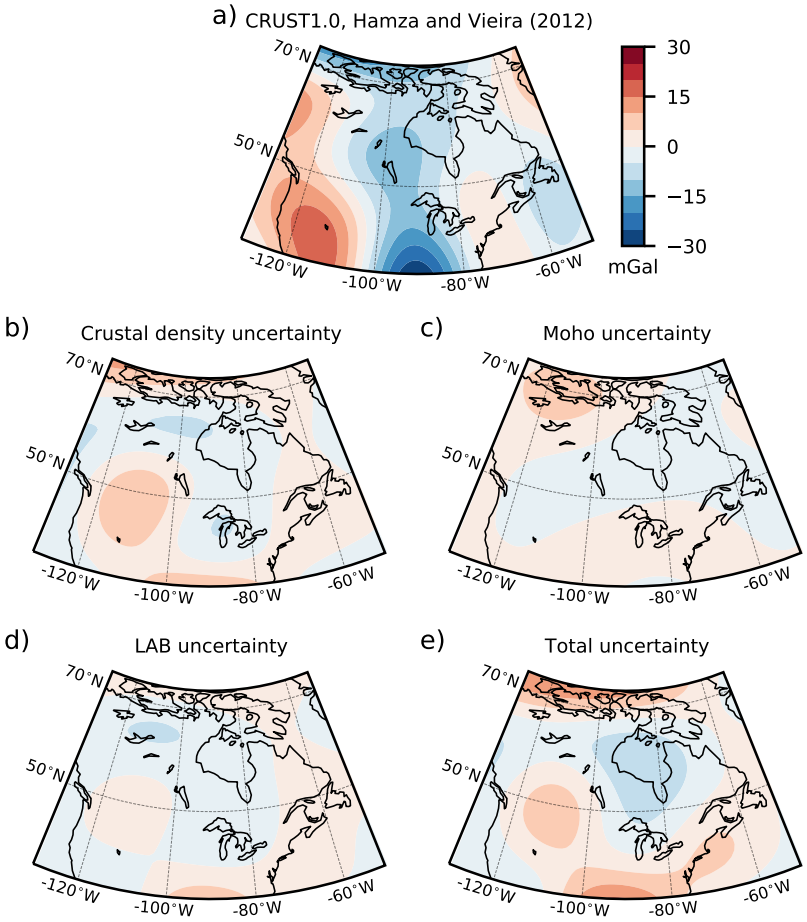

Figure 6. The effect of the crust on the gravity field (a), and the spread in gravity field due to the use of different crustal densities (b), Moho models (c), or LAB models (d). The total difference due to the combination of b, c and d is shown in (e).

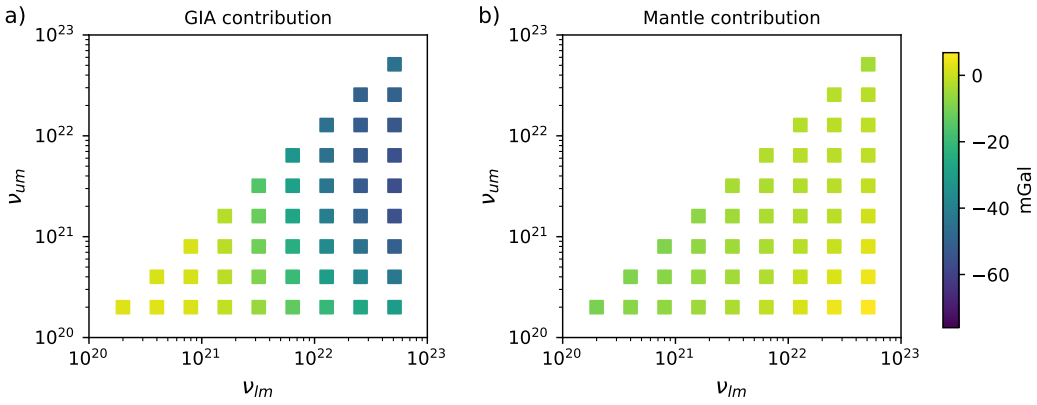

Figure 7. Contributions of GIA (a) and the mantle below 300 km (b) to the maximum of the anomaly in the static gravity field for different upper and lower mantle viscosities, in mGal, calculated at the location of the modelled maximum.

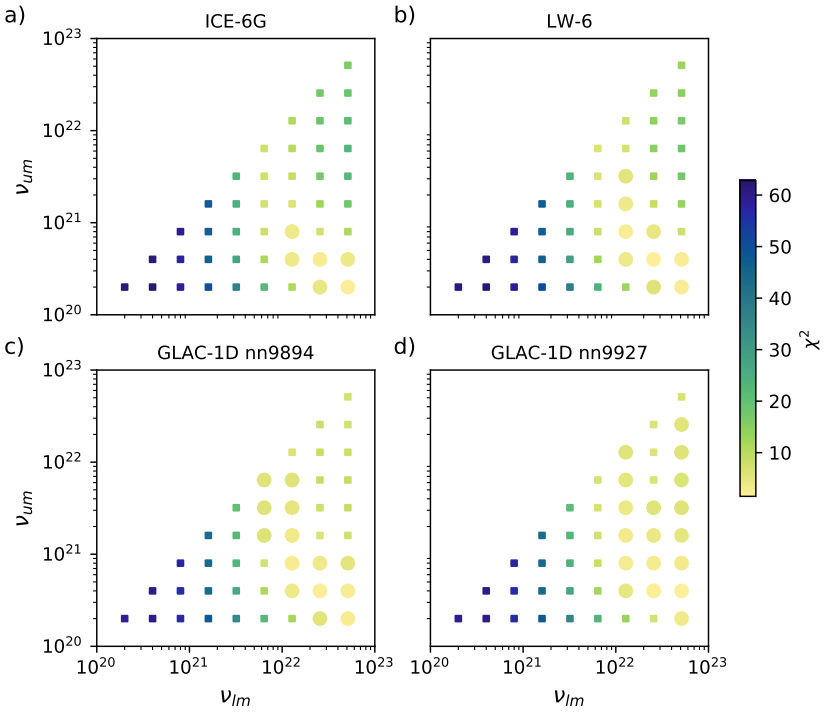

Figure 8. χ^2 misfit for different upper (ν_{um}) and lower (ν_{lm}) mantle viscosities. Each subplot is made using a different ice history: a) ICE-6G (Peltier et al., 2015; Argus et al., 2014), b) LW-6 (Lambeck et al., 2017), and c-d) two GLAC-1D ice histories (Tarasov et al., 2012). Models containing lower mantle viscosities $> 10^{22}$ Pa s perform better for all ice histories. The models that fit the data within 2.5 $\times$ the standard deviation are denoted by circles.

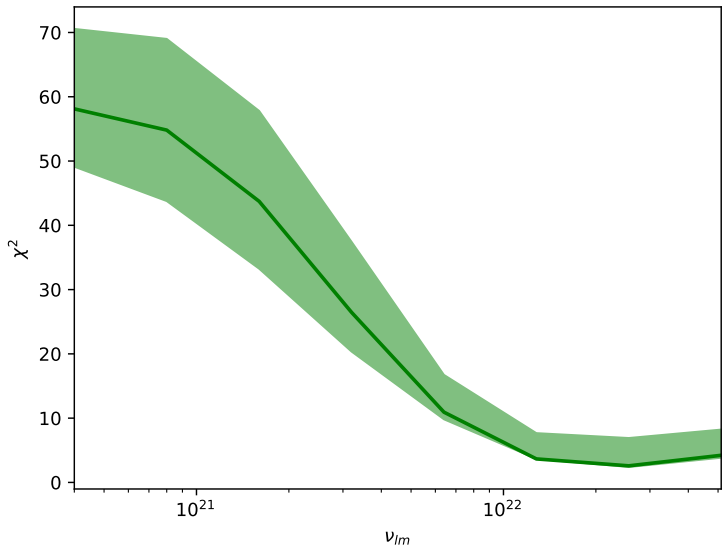

Figure 9. χ^2 misfit as a function of the lower mantle viscosity for different conversion factors in the mantle convection code. The dark green line shows the χ^2 misfit for a conversion factor of 0.15, the default value used in the study. The spread indicates the effect of varying the conversion factor between 0.1 and 0.4.

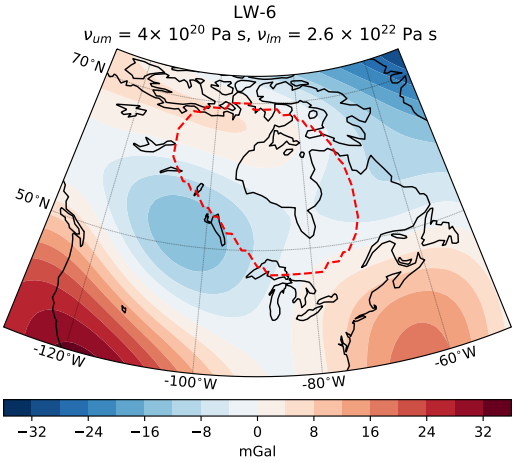

Figure 10. Long-wavelength gravity anomaly residual of the model containing the best fitting viscosity profile ($\nu_{um} = 4 \times 10^{20}$ Pa s, $\nu_{lm} = 2.6 \times 10^{22}$ Pa s) and ice history (LW-6). The red dashed line denotes the area used for the calculation of the misfit with the observed gravity field of XGM2016.

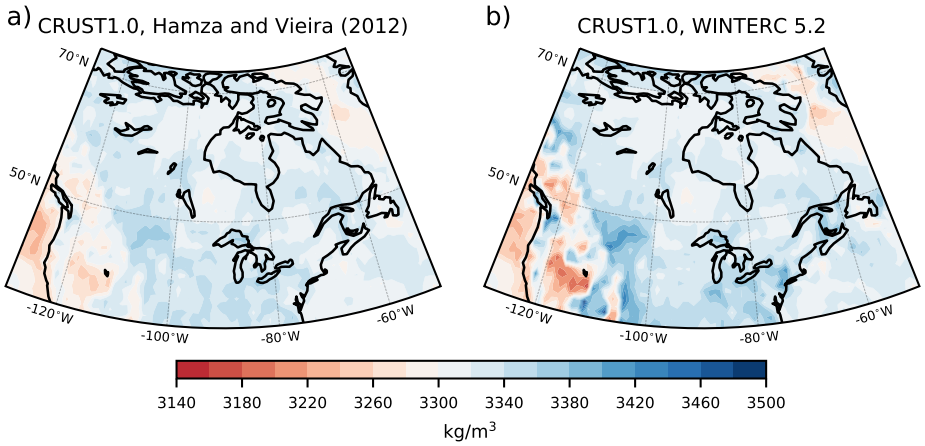

Figure A1. Lithospheric mantle densities after isostatic compensation using the CRUST1.0 crustal model and (a) the LAB from Hamza and Vieira (2012), or (b) the WINTERC 5.2 LAB.

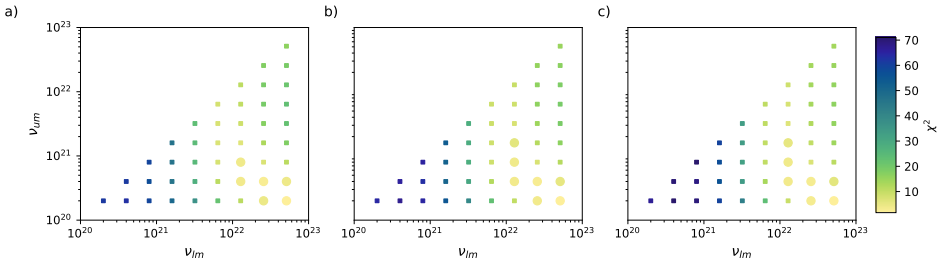

Figure B1. χ^2 misfit for different upper (ν_{um}) and lower (ν_{lm}) mantle viscosities. Results are shown for a lithospheric thickness of 80 km (a), 115 km (b), and 150 km (c). Models containing lower mantle viscosities $> 10^{22}$ Pa s perform better for all ice histories. The models that fit the data within 2.5 × the standard deviation are denoted by circles.

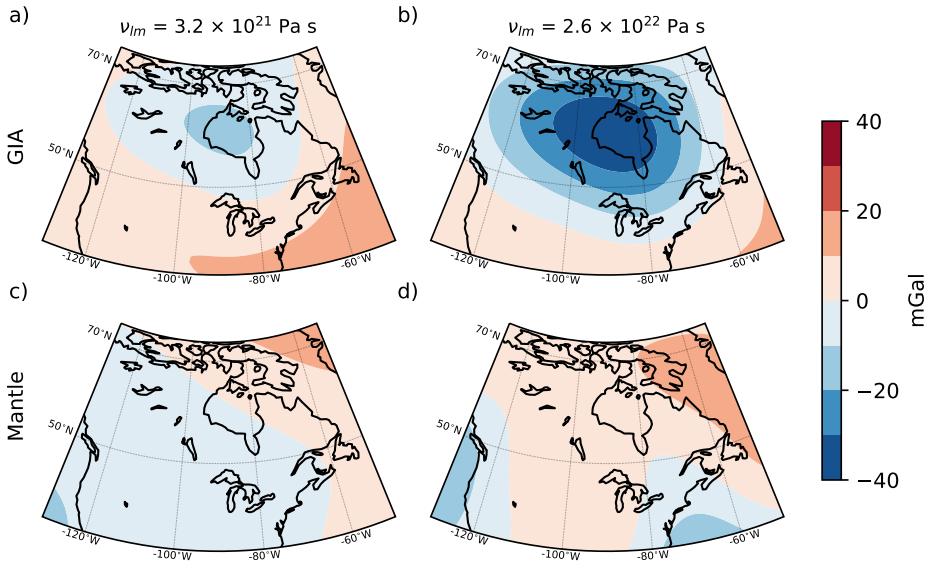

Figure C1. Effect of GIA (top row) and mantle convection (bottom row) on the gravity field for a lower mantle viscosity equal to 3.2 × 10 ^{21} Pa s (first column) and 2.6 × 10 ^{22} Pa s (second column). The viscosity of the upper mantle is the same across all subplots and equal to 4 × 10^{20} Pa s.

Acknowledgments

We would like to thank Lev Tarasov for providing us with the GLAC-1D models. We would like to thank Zdenek Martinec for making the FORTRAN-based spectral finite element code (SFEC), used for modelling mantle convection, available to us. Codes to run the crust-lithosphere-asthenosphere model and the GIA model are available at doi.org/10.4121/uuid:54c182ea-3826-4200-83d6-414dad27b289. The SFEC code for modelling mantle convection is available upon request from Zdenek Martinec. This study is funded by NWO under the project ALW.GO.2017.035.

References

A, G., Wahr, J., & Zhong, S. (2013, 11). Computations of the viscoelastic response of a 3-D compressible Earth to surface loading: an application to Glacial Isostatic Adjustment in Antarctica and Canada. *Geophysical Journal International*, *192*(2), 557-572. Retrieved from `https://doi.org/10.1093/gji/ggs030` doi: 10.1093/gji/ggs030

Afonso, J. C., Salajegheh, F., Szwillus, W., Ebbing, J., & Gaina, C. (2019). A global reference model of the lithosphere and upper mantle from joint inversion and analysis of multiple data sets. *Geophysical Journal International*, *217*(3), 1602–1628.

Argus, D. F., Peltier, W., Drummond, R., & Moore, A. W. (2014). The Antarctica component of postglacial rebound model ICE-6G_C (VM5a) based on GPS positioning, exposure age dating of ice thicknesses, and relative sea level histories. *Geophysical Journal International*, *198*(1), 537–563.

Auer, L., Boschi, L., Becker, T., Nissen-Meyer, T., & Giardini, D. (2014). Savani: A variable resolution whole-mantle model of anisotropic shear velocity variations based on multiple data sets. *Journal of Geophysical Research: Solid Earth*, *119*(4), 3006–3034.

Becker, T. W., & Boschi, L. (2002). A comparison of tomographic and geodynamic mantle models. *Geochemistry, Geophysics, Geosystems*, *3*(1).

Bower, D. J., Gurnis, M., & Seton, M. (2013). Lower mantle structure from paleogeographically constrained dynamic earth models. *Geochemistry, Geophysics, Geosystems*, *14*(1), 44–63.

Caron, L., Métivier, L., Greff-Lefftz, M., Fleitout, L., & Rouby, H. (2017). Inverting Glacial Isostatic Adjustment signal using Bayesian framework and two linearly relaxing rheologies. *Geophysical Journal International*, *209*(2), 1126–1147.

Cathles, L. (1975). The viscosity of the earth's mantle princeton university press. *New Jersey*, *390*.

Cianetti, S., Giunchi, C., & Spada, G. (2002). Mantle viscosity beneath the Hudson Bay: an inversion based on the Metropolis algorithm. *Journal of Geophysical Research: Solid Earth*, *107*(B12), ETG–12.

Čížková, H., van den Berg, A. P., Spakman, W., & Matyska, C. (2012). The viscosity of earth's lower mantle inferred from sinking speed of subducted lithosphere. *Physics of the earth and Planetary Interiors*, *200*, 56–62.

Dyke, A., & Prest, V. (1987). Late Wisconsinan and Holocene history of the Laurentide ice sheet. *Géographie physique et Quaternaire*, *41*(2), 237–263.

Dziewonski, A. M., & Anderson, D. L. (1981). Preliminary reference Earth model. *Physics of the earth and planetary interiors*, *25*(4), 297–356.

Eaton, D. W., & Darbyshire, F. (2010). Lithospheric architecture and tectonic evolution of the hudson bay region. *Tectonophysics*, *480*(1-4), 1–22.

Eaton, D. W., Darbyshire, F., Evans, R. L., Grütter, H., Jones, A. G., & Yuan, X. (2009). The elusive lithosphere–asthenosphere boundary (lab) beneath cratons. *Lithos*, *109*(1-2), 1–22.

Fischer, K. M., Ford, H. A., Abt, D. L., & Rychert, C. A. (2010). The lithosphere-asthenosphere boundary. *Annual Review of Earth and Planetary Sciences*, *38*, 551–575.

Flament, N., Gurnis, M., & Müller, R. D. (2013). A review of observations and models of dynamic topography. *Lithosphere*, *5*(2), 189–210.

Forte, A., & Mitrovica, J. X. (1996). New inferences of mantle viscosity from joint inversion of long-wavelength mantle convection and post-glacial rebound data. *Geophysical Research Letters*, *23*(10), 1147–1150.

Greff-Lefftz, M., & Legros, H. (1997). Some remarks about the degree-one deformation of the earth. *Geophysical Journal International*, *131*(3), 699–723.

Gu, Y. J., Dziewonski, A. M., Su, W., & Ekström, G. (2001). Models of the mantle shear velocity and discontinuities in the pattern of lateral heterogeneities. *Journal of Geophysical Research: Solid Earth*, *106*(B6), 11169–11199.

Gvirtzman, Z., Faccenna, C., & Becker, T. W. (2016). Isostasy, flexure, and dynamic topography. *Tectonophysics*, *683*, 255–271.

Hager, B. H., Clayton, R. W., Richards, M. A., Comer, R. P., & Dziewonski, A. M. (1985). Lower mantle heterogeneity, dynamic topography and the geoid. *Nature*, *313*(6003), 541.

Hamza, V., & Vieira, F. (2012). Global distribution of the lithosphere-asthenosphere boundary: a new look. *Solid Earth*, *3*(2), 199–212.

James, T. S. (1992). The hudson bay free-air gravity anomaly and glacial rebound. *Geophysical Research Letters*, *19*(9), 861–864.

Karato, S.-i. (1993). Importance of anelasticity in the interpretation of seismic tomography. *Geophysical Research Letters*, *20*(15), 1623–1626.

Karato, S.-i. (2008). Deformation of earth materials. *An Introduction to the Rheology of Solid Earth*, *463*.

Kaula, W. M. (1972). Global gravity and tectonics. *The nature of the solid Earth*, 385–405.

King, S. D. (1995). Radial models of mantle viscosity: results from a genetic algorithm. *Geophysical Journal International*, *122*(3), 725–734.

Kuchar, J., Milne, G., & Latychev, K. (2019). The importance of lateral Earth structure for North American glacial isostatic adjustment. *Earth and Planetary Science Letters*, *512*, 236–245.

Lachenbruch, A. H., & Morgan, P. (1990). Continental extension, magmatism and elevation; formal relations and rules of thumb. *Tectonophysics*, *174*(1-2), 39–62.

Lambeck, K., Purcell, A., & Zhao, S. (2017). The North American Late Wisconsin ice sheet and mantle viscosity from glacial rebound analyses. *Quaternary Science Reviews*, *158*, 172–210.

Lambeck, K., Rouby, H., Purcell, A., Sun, Y., & Sambridge, M. (2014). Sea level and global ice volumes from the Last Glacial Maximum to the Holocene. *Proceedings of the National Academy of Sciences*, *111*(43), 15296–15303.

Laske, G., Masters, G., Ma, Z., & Pasyanos, M. (2013). Update on CRUST1. 0—A 1-degree global model of Earth's crust. In *Geophys. res. abstr* (Vol. 15, p. 2658).

Li, T., Wu, P., Wang, H., Steffen, H., Khan, N. S., Engelhart, S. E., ... Horton, B. P. (2020). Uncertainties of glacial isostatic adjustment model predictions in north america associated with 3d structure. *Geophysical Research Letters*, e2020GL087944.

Liu, X., & Zhong, S. (2016). Constraining mantle viscosity structure for a thermochemical mantle using the geoid observation. *Geochemistry, Geophysics, Geosystems*, *17*(3), 895–913.

Martinec, Z., Klemann, V., van der Wal, W., Riva, R., Spada, G., Sun, Y., ... others (2018). A benchmark study of numerical implementations of the sea level equation in gia modelling. *Geophysical Journal International*, *215*(1), 389–414.

Métivier, L., Caron, L., Greff-Lefftz, M., Pajot-Métivier, G., Fleitout, L., & Rouby, H. (2016). Evidence for postglacial signatures in gravity gradients: A clue in lower mantle viscosity. *Earth and Planetary Science Letters*, *452*, 146–156.

Milne, G. A., & Mitrovica, J. X. (1998). Postglacial sea-level change on a rotating earth. *Geophysical Journal International*, *133*(1), 1–19.

Mitrovica, J., Davis, J., & Shapiro, I. (1994). A spectral formalism for computing three-dimensional deformations due to surface loads: 2. Present-day glacial isostatic adjustment. *Journal of Geophysical Research: Solid Earth*, *99*(B4), 7075–7101.

Mitrovica, J., & Forte, A. (2004). A new inference of mantle viscosity based upon joint inversion of convection and glacial isostatic adjustment data. *Earth and Planetary Science Letters*, *225*(1-2), 177–189.

Mitrovica, J., & Peltier, W. (1991a). Free air gravity anomalies associated with glacial isostatic disequilibriu: Load history effects on the inference of deep mantle viscosity. *Geophysical Research Letters*, *18*(2), 235–238.

Mitrovica, J., & Peltier, W. (1991b). On postglacial geoid subsidence over the equatorial oceans. *Journal of Geophysical Research: Solid Earth*, *96*(B12), 20053–20071.

Nakada, M., & Okuno, J. (2016). Inference of mantle viscosity for depth resolutions of gia observations. *Geophysical Supplements to the Monthly Notices of the Royal Astronomical Society*, *207*(2), 719–740.

Pail, R., Fecher, T., Barnes, D., Factor, J., Holmes, S., Gruber, T., & Zingerle, P. (2018). Short note: the experimental geopotential model XGM2016. *Journal of Geodesy*, *92*(4), 443–451.

Paulson, A., Zhong, S., & Wahr, J. (2005). Modelling post-glacial rebound with lateral viscosity variations. *Geophysical Journal International*, *163*(1), 357–371.

Paulson, A., Zhong, S., & Wahr, J. (2007). Inference of mantle viscosity from GRACE and relative sea level data. *Geophysical Journal International*, *171*(2), 497–508.

Peltier, W., Argus, D., & Drummond, R. (2015). Space geodesy constrains ice age terminal deglaciation: The global ICE-6G_C (VM5a) model. *Journal of Geophysical Research: Solid Earth*, *120*(1), 450–487.

Peltier, W., & Drummond, R. (2008). Rheological stratification of the lithosphere: A direct inference based upon the geodetically observed pattern of the glacial isostatic adjustment of the north american continent. *Geophysical Research Letters*, *35*(16).

Peltier, W., Forte, A., Mitrovica, J., & Dziewonski, A. (1992). Earth's gravitational field: seismic tomography resolves the enigma of the laurentian anomaly. *Geophysical Research Letters*, *19*(15), 1555–1558.

Perry, H., Forte, A., & Eaton, D. (2003). Upper-mantle thermochemical structure below north america from seismic–geodynamic flow models. *Geophysical Journal International*, *154*(2), 279–299.

Ritsema, J., Deuss, a. A., Van Heijst, H., & Woodhouse, J. (2011). S40RTS: a degree-40 shear-velocity model for the mantle from new Rayleigh wave dispersion, teleseismic traveltime and normal-mode splitting function measurements. *Geophysical Journal International*, *184*(3), 1223–1236.

Root, B., Ebbing, J., van der Wal, W., England, R., & Vermeersen, L. (2017). Comparing gravity-based to seismic-derived lithosphere densities: a case study of the British Isles and surrounding areas. *Geophysical Journal International*, *208*(3), 1796–1810.

Root, B., Novák, P., Dirkx, D., Kaban, M., van der Wal, W., & Vermeersen, L. (2016). On a spectral method for forward gravity field modelling. *Journal of Geodynamics*, *97*, 22–30.

Root, B., van der Wal, W., Novák, P., Ebbing, J., & Vermeersen, L. (2015). Glacial isostatic adjustment in the static gravity field of Fennoscandia. *Journal of Geophysical Research: Solid Earth*, *120*(1), 503–518.

Rudolph, M. L., Lekić, V., & Lithgow-Bertelloni, C. (2015). Viscosity jump in earth's mid-mantle. *Science*, *350*(6266), 1349–1352.

Sasgen, I., Klemann, V., & Martinec, Z. (2012). Towards the inversion of GRACE gravity fields for present-day ice-mass changes and glacial-isostatic adjustment in North America and Greenland. *Journal of Geodynamics*, *59*, 49–63.

Schetselaar, E., & Snyder, D. (2017). National database of MOHO depth estimates from seismic refraction and teleseismic surveys. *Geological Survey of Canada*, *Open File 8243*(1 .zip file). doi: https://doi.org/10.4095/305396

Schotman, H. H. A. (2008). *Shallow-earth rheology from glacial isostasy and satellite gravity: a sensitivity analysis for goce* (Unpublished doctoral dissertation). Delft University of Technology.

Sigloch, K. (2011). Mantle provinces under north america from multifrequency p wave tomography. *Geochemistry, Geophysics, Geosystems*, *12*(2).

Simmons, N. A., Forte, A. M., Boschi, L., & Grand, S. P. (2010). GyPSuM: A joint tomographic model of mantle density and seismic wave speeds. *Journal of Geophysical Research: Solid Earth*, *115*(B12).

Simons, M., & Hager, B. H. (1997). Localization of the gravity field and the signature of glacial rebound. *Nature*, *390*(6659), 500–504.

Sleep, N. H. (2005). Evolution of the continental lithosphere. *Annu. Rev. Earth Planet. Sci.*, *33*, 369–393.

Soldati, G., Boschi, L., Deschamps, F., & Giardini, D. (2009). Inferring radial models of mantle viscosity from gravity (GRACE) data and an evolutionary algorithm. *Physics of the Earth and Planetary Interiors*, *176*(1-2), 19–32.

Steffen, H., Müller, J., & Denker, H. (2009). Analysis of mass variations in northern glacial rebound areas from GRACE data. In *Observing our changing earth* (pp. 501–509). Springer.

Steinberger, B. (2007). Effects of latent heat release at phase boundaries on flow in the Earth's mantle, phase boundary topography and dynamic topography at

the Earth's surface. *Physics of the Earth and Planetary Interiors*, *164*(1-2), 2–20.

Steinberger, B., & Calderwood, A. R. (2006). Models of large-scale viscous flow in the Earth's mantle with constraints from mineral physics and surface observations. *Geophysical Journal International*, *167*(3), 1461–1481.

Steinberger, B., Conrad, C. P., Tutu, A. O., & Hoggard, M. J. (2019). On the amplitude of dynamic topography at spherical harmonic degree two. *Tectonophysics*, *760*, 221–228.

Stokes, C. R. (2017). Deglaciation of the Laurentide Ice Sheet from the Last Glacial Maximum. *Cuadernos de investigación geográfica.*, *43*(2), 377–428.

Su, W.-j., & Dziewonski, A. M. (1991). Predominance of long-wavelength heterogeneity in the mantle. *Nature*, *352*(6331), 121–126.

Szwillus, W., Afonso, J. C., Ebbing, J., & Mooney, W. D. (2019). Global crustal thickness and velocity structure from geostatistical analysis of seismic data. *Journal of Geophysical Research: Solid Earth*, *124*(2), 1626–1652.

Tamisiea, M., Mitrovica, J., & Davis, J. (2007). GRACE gravity data constrain ancient ice geometries and continental dynamics over Laurentia. *Science*, *316*(5826), 881–883.

Tarasov, L., Dyke, A. S., Neal, R. M., & Peltier, W. R. (2012). A data-calibrated distribution of deglacial chronologies for the North American ice complex from glaciological modeling. *Earth and Planetary Science Letters*, *315*, 30–40.

Tosi, N. (2008). *Numerical modeling of present-day mantle convection* (Unpublished doctoral dissertation). Univerzita Karlova, Matematicko-fyzikální fakulta.

Trampert, J., Deschamps, F., Resovsky, J., & Yuen, D. (2004). Probabilistic tomography maps chemical heterogeneities throughout the lower mantle. *Science*, *306*(5697), 853–856.

Van der Meer, D. G., Van Hinsbergen, D. J., & Spakman, W. (2018). Atlas of the underworld: Slab remnants in the mantle, their sinking history, and a new outlook on lower mantle viscosity. *Tectonophysics*, *723*, 309–448.

van der Wal, W., Braun, A., Wu, P., & Sideris, M. G. (2009). Prediction of decadal slope changes in Canada by glacial isostatic adjustment modelling. *Canadian Journal of Earth Sciences*, *46*(8), 587–595.

van der Wal, W., Wu, P., Sideris, M. G., & Shum, C. (2008). Use of GRACE determined secular gravity rates for glacial isostatic adjustment studies in North-America. *Journal of Geodynamics*, *46*(3-5), 144–154.

Vermeersen, L., & Sabadini, R. (1997). A new class of stratified viscoelastic models by analytical techniques. *Geophysical Journal International*, *129*(3), 531–570.

Walcott, R. I. (1973). Structure of the earth from glacio-isostatic rebound. *Annual Review of Earth and Planetary Sciences*, *1*(1), 15–37.

Wang, H., & Wu, P. (2006). Effects of lateral variations in lithospheric thickness and mantle viscosity on glacially induced surface motion on a spherical, self-gravitating maxwell earth. *Earth and Planetary Science Letters*, *244*(3-4), 576–589.

Watts, A. B. (2001). *Isostasy and Flexure of the Lithosphere*. Cambridge University Press.

Watts, A. B., & Moore, J. D. P. (2017). Flexural isostasy: Constraints from gravity and topography power spectra. *Journal of Geophysical Research: Solid Earth*, *122*(10), 8417–8430.

Wieczorek, M. A., & Meschede, M. (2018). Shtools: Tools for working with spherical harmonics. *Geochemistry, Geophysics, Geosystems*, *19*(8), 2574–2592.

Wolf, D., Klemann, V., Wünsch, J., & Zhang, F.-p. (2006). A reanalysis and reinterpretation of geodetic and geological evidence of glacial-isostatic adjustment in the Churchill region, Hudson Bay. *Surveys in Geophysics*, *27*(1), 19–61.

Wu, P. (2005). Effects of lateral variations in lithospheric thickness and mantle viscosity on glacially induced surface motion in laurentia. *Earth and Planetary*

Science Letters, *235*(3-4), 549–563.

Wu, P. (2006). Sensitivity of relative sea levels and crustal velocities in Laurentide to radial and lateral viscosity variations in the mantle. *Geophysical Journal International*, *165*(2), 401–413.

Wu, P., & Peltier, W. (1982). Viscous gravitational relaxation. *Geophysical Journal International*, *70*(2), 435–485.

Wu, P., & Peltier, W. (1983). Glacial isostatic adjustment and the free air gravity anomaly as a constraint on deep mantle viscosity. *Geophysical Journal International*, *74*(2), 377–449.

Wu, P., & Peltier, W. (1984). Pleistocene deglaciation and the earth's rotation: a new analysis. *Geophysical Journal International*, *76*(3), 753–791.

Zhao, S. (2013). Lithosphere thickness and mantle viscosity estimated from joint inversion of GPS and GRACE-derived radial deformation and gravity rates in North America. *Geophysical Journal International*, *194*(3), 1455–1472.